第43卷第3期
2024年6月

红 外 与 毫 米 波 学 报
J. Infrared Millim. Waves

Vol. 43, No. 3
June, 2024

文章编号：1001-9014(2024)03-0314-08　　DOI:10.11972/j.issn.1001-9014.2024.03.004

Ultrasensitive and broad-spectrum photodetectors based on InSe/$MoTe_2$ heterostructure

XING Yan-Hui[1*], HE Wen-Xin[1,3], HAN Zi-Shuo[1], GUAN Bao-Lu[1], MA Hai-Xin[1,3], MA Xiao-Hui[2], HAN Jun[1], SHI Wen-Hua[3], ZHANG Bao-Shun[3], LYU Wei-Ming[3*], ZENG Zhong-Ming[3]

(1. Key Laboratory of Opto-electronics Technology, Ministry of Education, College of Microelectronics, Beijing University of Technology, Beijing 100124, China;
2. State key Laboratory of High Power semiconductor laser of Changchun University of Science and Technology, Changchun 130022, China;
3. Nanofabrication facility, Suzhou Institute of Nano-Tech and Nano-Bionics, Chinese Academy of Sciences, Suzhou 215123, China)

Abstract: The photogating effect based on the vertical structure of a two-dimensional material allows high-sensitivity and broad-spectrum photodetector. A high-sensitivity photodetector based on the vertical heterostructure of indium selenide (InSe)/molybdenum ditelluride ($MoTe_2$) is reported, which exhibits excellent broad-spectrum detection capability from 365 to 965 nm. The top layer of InSe was used as the grating layer to regulate the channel current, and $MoTe_2$ was used as the transmission layer. By combining the advantages of the two materials, the photodetector has a fast response time of 21.6 ms and achieves a maximum detectivity of 1.05×10^{13} Jones under 365 nm laser irradiation. Under the illumination of 965 nm, the detectivity still achieves the order of 10^9 Jones. In addition, the InSe/$MoTe_2$ heterostructure exhibits an external quantum efficiency of 1.03×10^5%, demonstrating strong photoelectric conversion capability.

Key words: two-dimensional material, broadband photodetectors, photogating effect, ultrasensitive

基于InSe/$MoTe_2$异质结构的超灵敏宽光谱光电探测器

邢艳辉[1*]，贺雯馨[1,3]，韩梓硕[1]，关宝璐[1]，马海鑫[1,3]，马晓辉[2]，韩　军[1]，时文华[3]，张宝顺[3]，吕伟明[3*]，曾中明[3]

(1. 北京工业大学 微电子学院 光电子技术教育部重点实验室，北京 100124；
2. 长春理工大学 高功率半导体激光国家重点实验室，吉林 长春 130022；
3. 中国科学院 苏州纳米技术与纳米仿生研究所 纳米加工平台，江苏 苏州 215123)

摘要：基于光栅效应的二维材料垂直结构可实现高灵敏度和宽光谱光探测器。本文报告了一种基于硒化铟(InSe)/二碲化钼($MoTe_2$)垂直异质结构的高灵敏度光电探测器，该探测器在365~965 nm波长范围内具有出色的宽光谱探测能力。顶层的InSe用作调节沟道电流的光栅层，$MoTe_2$则用作传输层。通过结合两种材料的优势，该光电探测器的响应时间为21.6 ms，比探测率在365 nm光照下可以达到1.05×10^{13} Jones，在965nm光照下也可达到10^9 Jones数量级。外量子效率可达1.03×10^5%，显示出强大的光电转换能力。

关　键　词：二维材料；宽带光电探测器；光栅效应；超灵敏

中图分类号：TN214　　**文献标识码**：A

Received date: 2023-07-26, **revised date**: 2024-03-02　　**收稿日期**：2023-07-26，**修回日期**：2024-03-02

Foundation items: Supported by the National Natural Science Foundation of China (No. 60908012, 61575008, 61775007, 61874145, 62074011, 62134008); National Key Research and Development Program of China (No. 2018YFA0209000, 2021YFC2203400, 2021YFA1200804); the Beijing Natural Science Foundation (No. 4172011, 4202010) and Beijing Nova Program (Z201100006820096).

Biography: XING Yan-Hui (1972-), female, JiLin, China, associate professor, Doctor. Research area involves Semiconductor materials and devices. Email: xingyanhui@bjut.edu.cn

[*] **Corresponding author**: Email: xingyanhui@bjut.edu.cn; wmlv2015@sinano.ac.cn

Introduction

Two-dimensional (2D) materials, such as graphene, BP, and transition metal dichalcogenides (TMDCs), the research of 2D materials has become a top priority in the field of optoelectronics due to their excellent optical and electrical properties[1]. TMDCs materials have high mobility and high On/Off ratios because they can achieve large modulation through the gate field effect[2]. These characteristics enable them to be widely used in photodetectors. However, most photodetectors based on TMDCs, such as those based on $MoTe_2$ and WSe_2, can only operate in the visible region due to their relatively large bandgap[3-5]. Therefore, it is significant to explore and manufacture photodetectors with a broader spectrum, higher sensitivity and high responsivity using two-dimensional materials.

2D van der Waals (vdW) heterojunctions offer an ideal platform to overcome the limitations of single materials and enhance device performance. In vdW heterojunctions, the individual components are stacked using weak vdW forces between the layers[6-7], effectively avoiding the limitations of lattice matching and other factors in traditional heterojunctions. In recent years, the bandgap of $MoTe_2$ materials has been found to range from 0.83 eV for bulk materials to 1.1 eV for monolayers[8-9], which is narrower than that of other commonly used TMDCs materials such as MoS_2 and ReS_2[10]. Broad-spectrum photodetectors (600-1550 nm) based on $MoTe_2$ materials have been successfully demonstrated. L. Yin[11] reported a multilayer $MoTe_2$ device with high responsivity to visible light at large back-gate voltages. However, the device's detectivity may be severely degraded due to its high dark current. Previous studies have utilized various materials, such as MoS_2[12], graphene[13], and Ge[14], to form heterojunction photodetectors with $MoTe_2$. The high carrier mobility of $MoTe_2$ enables the photodetectors to have faster response times[15]. In addition, indium selenide (InSe) has recently gained attention in optoelectronics and nanoelectronics due to its high electron mobility and broadband optical absorption. The InSe-based photodetectors exhibit outstanding performance in broadband photodetection (400-1000 nm) and fast response times, as low as 87 μs[16-18]. This combination of InSe and $MoTe_2$ advantages enhances the overall performance of the photodetector. Currently, there is limited research on the photodetection capability of $InSe/MoTe_2$ heterojunctions. Sun el. [19] proposed an $InSe/MoTe_2$ heterojunction photodetector for photodetection under two types of laser irradiation, 405 nm and 635 nm. The photodetector achieved high detectivity, but the maximum responsivity was limited to 15.4 mA/W.

In this paper, a photodetector based on $InSe/MoTe_2$ vertical heterojunction is fabricated, in which $MoTe_2$ serves as the transmission layer and InSe serves as the grating layer to regulate the channel current. The photodetector exhibits excellent photodetection performance due to its vertical structure and high-quality interface. The detectivity of the photodetector shows an ultrahigh value of over 1.05×10^{13} Jones, surpassing that of other reported photodetectors based on 2D materials[12-14,20-25]. Ultraviolet (100-400 nm) photodetectors have attracted extensive attention in many fields, such as space exploration, biological analysis, environmental sensors, communication, and imaging[26]. In addition, the photodetectors reported in this paper have photoresponses ranging from ultraviolet (365 nm) to near-infrared (965 nm). The photodetector exhibits an ultra-high external quantum efficiency (EQE) of 1.03×10^5%, resulting in extremely high photoelectric conversion. By modulating the gate voltage, the responsivity can reach 300.57 A/W. The heterojunction photodetector also exhibits outstanding detection performances with a fast response.

1 Device fabrication and characterization

The vertically structured $InSe/MoTe_2$ heterojunction was fabricated using a deterministic dry transferred technique. First, 300 nm silicon oxide insulation layer was deposited on a silicon wafer by plasma-enhanced chemical vapor deposition. The BN thin layer was removed by mechanical stripping and placed on the SiO_2/Si substrate to provide a clean and flat interface. Then $MoTe_2$ nanoflakes were mechanically exfoliated from the bulk crystals to the polydimethylsiloxane (PDMS) films and transferred onto the SiO_2/Si substrate. Next, several layers of mechanical peeling InSe flakes were artificially stacked on the $MoTe_2$ flakes under the optical microscope (OM, BX51, OLMPUS) assisted by an aligned transfer system. The two-dimensional materials mentioned in the text are commercially available bulk crystals. Finally, multiple electrode patterns were defined by standard electron beam lithography (EBL, Raith eLine Plus), then Ti/Au (10 nm/60 nm) metal stacks were deposited by electron beam evaporation (Ulvac Ei-5z) to form source and drain electrodes. The thickness of the photodetector was determined by AFM (Dimension ICON, American Bruker). Raman spectra were carried out using a Raman spectrometer system (Raman, LABRAM HR, Japan Horriba-JY) with a 532 nm laser source. The atomic structure features of the heterojunction were examined using HRTEM (Talos). The composition and element distribution of the heterojunction were analyzed via EDS mapping on the HRTEM. Before the HRTEM test, the photodetector's surface was coated with a conductive layer of elemental Cr to facilitate the positioning of the cut sample and the deposition of the protective layer under the focused ion beam (FIB) microscope. The electrical transport properties of the photodetector were carried out by Keithley 2612B and 2400 at room temperature.

2 Results and Discussion

The vertically stacked heterostructure based on $InSe/MoTe_2$ is shown in Fig. 1(a). The Ti/Au electrodes were placed on the $MoTe_2$. The thicknesses of the $MoTe_2$ and InSe flakes are 8 nm and 15 nm, respectively, as shown in Fig. 1(b) and (c). The morphological characteristics of the $InSe/MoTe_2$ heterojunction are shown in the inset of Fig. 1(b), which displays a flat surface that did not sus-

tain any damage during material peeling and transfer. Fig. 1(d) shows the results of high-resolution transmission electron microscopy (HRTEM). The interfaces of all layers are clear, flat, and uncontaminated, indicating good interface quality. The thickness of each layer has been verified, and is consistent with the AFM test results. Fig. 1(e) shows the detailed energy-dispersive X-ray spectroscopy (EDS) elemental mapping, which demonstrates uniform distribution of all elements in the $MoTe_2$ and InSe layers without diffusion. Raman spectra of individual materials and the overlapped region are displayed in Fig. 1(f). Specifically, for pristine InSe (red line), four prominent peaks are centered at 116 cm^{-1}, 178 cm^{-1}, 200 cm^{-1} and 227 cm^{-1}, corresponding to A_1', E''(TO), E''(LO), and A_1 modes[27]. The Raman signatures of $MoTe_2$ (green line) are typically observed at 232 cm^{-1} (E^1_{2g}), 171 cm^{-1} (A_{1g}), and 288 cm^{-1} (B^1_{2g})[28]. These peaks were also observed in the spectra of the overlapped region, indicating good quality of thin flakes in the junction region after layer exfoliation and device fabrication.

The electrical properties of the InSe/$MoTe_2$ heterojunction photodetector were tested under dark conditions. Fig. 2 shows the electrical characteristic curve of the InSe/$MoTe_2$ heterojunction photodetector with an increase in the back gate voltage from -60 to 60 V. The output characteristic curve (I_{ds}−V_{ds}) of the InSe/$MoTe_2$ heterojunction photodetector is shown in Fig. 2(a). As the current increases and the temperature rises, the resistance of the device also increases[27,29], resulting in nonlinearity in the output characteristics. Fig. 2(b) shows the transfer characteristic curve (I_{ds}−V_g) of the InSe/$MoTe_2$ heterojunction device in the dark state. The current of the device initially decreases and then increases with the gate voltage changing, indicating that the device exhibits bipolar behavior.

To investigate the optoelectronic performance of InSe/$MoTe_2$ heterojunction photodetectors under the illumination, we measured the I_{ds}−V_{ds} curves (Fig. 3(b)) and the I_{ds}−V_g curves (Fig. 3(c)) of InSe/$MoTe_2$ heterojunction devices at different incident optical powers density under 365nm light source (V_g=0 V). Fig. 3(a) shows a schematic diagram of the device under laser irradiation. The output *I*-*V* curve in Fig. 3(b) demonstrates that the current in the channel increases as the incident optical power density increases. This indicates that more photogenerated carriers are produced in the channel with an increase in incident optical power density. Additionally, the photocurrent I_{ph} (I_{ph}=$I_{illumination}$−I_{dark}) is positively correlated with V_{ds} (where $I_{illumination}$ and I_{dark} are I_{ds} with and without illumination). Fig. 3(c) shows the I_{ds}−V_g curves. The current in the channel is positively correlated with the incident optical power density. The I_{ds} of the device increases significantly under laser irradiation, indicating that the photocurrent always dominates throughout the operating range of the device. In the conducting state (when V_g>V_{th}), the built-in field of the heterojunction increases as the Fermi level of $MoTe_2$ shifts in the conduction band due to the accumulation of electrons, leading to more efficient electron-hole pairs separation and an increase in the optical response[30]. The energy band diagram of the electrical transport mechanism of the

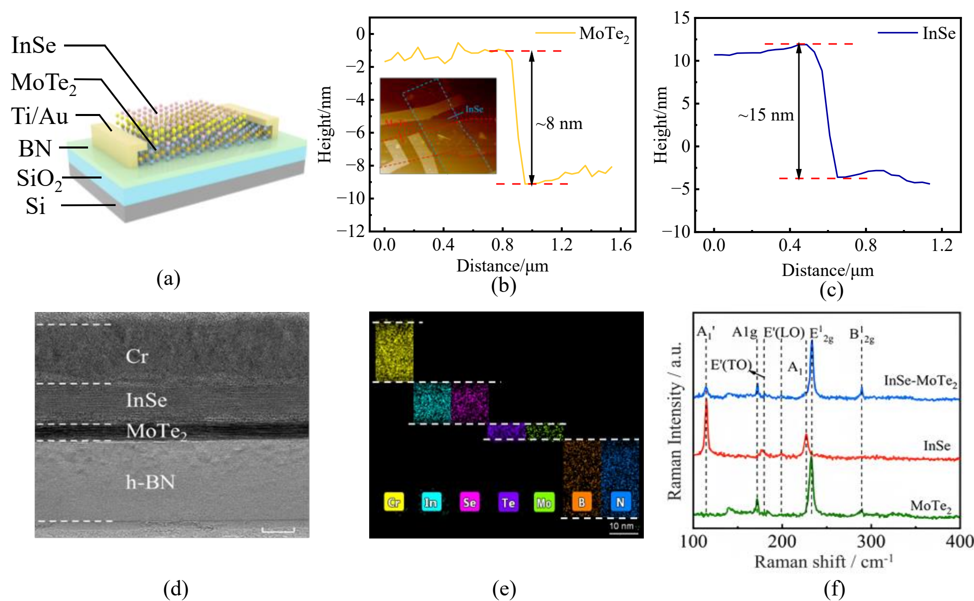

Fig. 1 Characterization of InSe/$MoTe_2$ heterostructure: (a) Schematic diagram of the InSe/$MoTe_2$ heterostructure; (b) The AFM image of $MoTe_2$ flakes. Inset: morphological characteristics of the InSe/$MoTe_2$ heterojunction; (c) The AFM image of InSe flakes; (d) HRTEM image; (e) EDS of the corresponding elements of the photodetector; (f) Raman spectra of pristine InSe, $MoTe_2$ and overlapped region.

图1 InSe/$MoTe_2$异质结构的表征:(a) InSe/$MoTe_2$异质结构示意图;(b) $MoTe_2$材料的AFM图像,插图:InSe/$MoTe_2$异质结的形貌特征图;(c) InSe材料的AFM图像;(d) HRTEM图像;(e) 光电探测器各层元素的EDS图像;(f) 原始InSe、$MoTe_2$和重叠区域的拉曼光谱

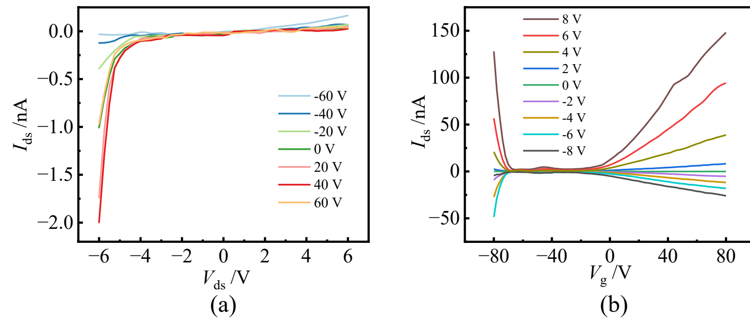

Fig. 2 Electrical *I-V* characteristics of the device based on InSe/$MoTe_2$ heterostructure under non-illumination condition: (a) I_{ds}-V_{ds} output characteristics under various back gate voltages; (b) I_{ds}-V_g transfer curves at various drain voltages.
图2 基于InSe/MoTe2异质结构器件在无光照条件下的电学*I-V*特性:(a) 不同背栅电压下的I_{ds}-V_{ds}输出特性曲线;(b) 不同漏极电压下的I_{ds}-V_g转移特性曲线

device is shown in Figure S1 (Supporting Information).

The non-linear relationship between the photocurrent and optical power density can be well fitted with the power law equation[31]:

$$I_{ph} = aP^{\theta} \quad , \quad (1)$$

where a is a constant for a certain wavelength, P is the incident power density and the exponent θ determines the photoelectric conversion efficiency. Fig. 3(d) shows the relationship between photocurrent and different incident power density at V_{ds}=6 V. As the incident power density increases, the photocurrent in the channel also increases. The photocurrent data can be well fitted with incident power density, and the obtained θ value of 0.93 (<1) verifies the presence of the photogating effect[32]. Demonstrating the presence of carrier trapping in the top InSe layer to photocurrent as a grating layer, inducing more electron production in the channel to further modulate the channel conductance.

To evaluation the performance of the heterojunction photodetector, the responsivity (R), detectivity (D^*), external quantum efficiency (EQE), and response time (τ) as evaluation metrics, which are be defined by the

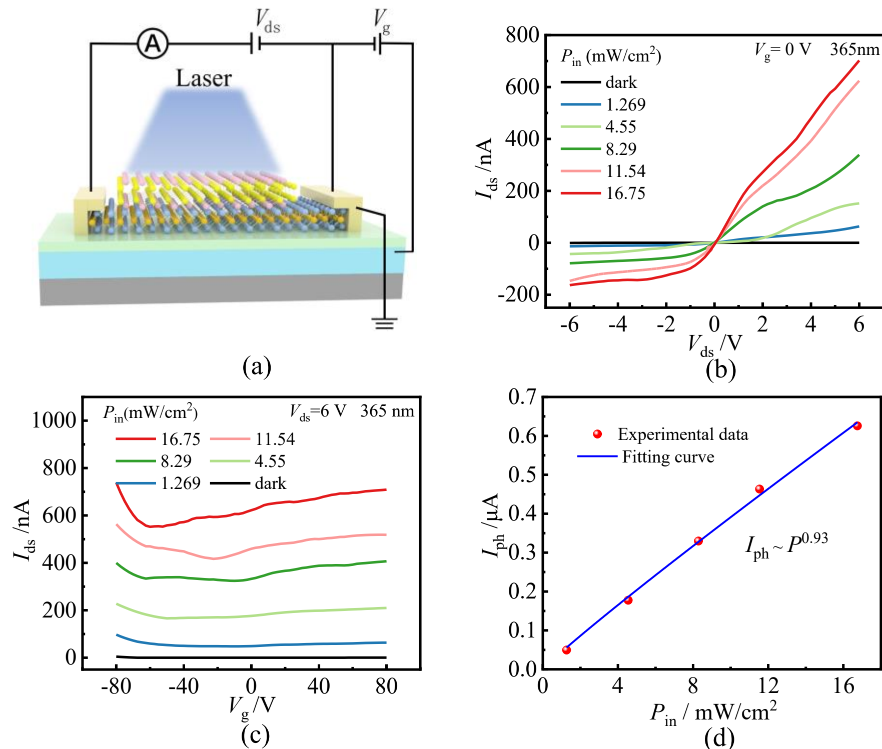

Fig. 3 (a) Schematic structure of the device under laser irradiation; (b)Photo-response of the I_{ds}-V_{ds} output characteristics with different incident light power under 365 nm illumination (V_g = 0 V); (c) Photo-response of the I_{ds}-V_g transfer characteristics with different incident light power under 365 nm illumination (V_{ds} = 6 V); (d) The I_{ph} as a function of incident light power at V_{ds} = 6 V
图3 (a)激光照射下的器件结构示意图;(b) 在365 nm光照下不同入射光功率的I_{ds}-V_{ds}输出特性曲线(V_g = 0 V);(c) 在365 nm光照下 不同入射光功率下I_{ds}-V_g转移特性曲线(V_{ds} = 6 V);(d) Vds = 6 V时,I_{ph}与入射光功率的函数关系

following equations:

$$R = I_{ph}/P_{in}A \quad , \quad (2)$$

$$D^* = RA^{1/2}/(2eI_{dark})^{1/2} \quad , \quad (3)$$

$$EQE = hcR\lambda^{-1}e^{-1} \quad , \quad (4)$$

$$NEP = A^{1/2}/D^* \quad , \quad (5)$$

where P_{in} is the incident optical power density, A is the effective illumination area, c is the speed of light, λ is the incident light wavelength and h is Planck's constant.

Fig. 4(a) shows the relationship between responsivity and gate voltage under different optical power density when V_{ds}=6 V. The responsivity decreases with increasing incident light power, which is consistent with previous studies[32]. It's mainly due to the enhancement of carrier scattering and recombination rates under higher incident light power densities. The InSe/$MoTe_2$ heterojunction photodetectors exhibit a responsivity of 300.57 A/W when V_g=-80 V and P_{in}=1.269 mW/cm². Fig. 4(b) shows the relationship between detectivity and incident light power density. Detectivity decreases as incident light power density increases. The highest detectivity of 1.05×10^{13} Jones was obtained at V_{ds} = 6 V, V_g = -15 V, and P_{in} = 1.269 mW/cm². The high detectivity can be mainly attributed to the arrangement of the heterojunction energy bands, which allows the electrons in $MoTe_2$ to naturally flow into InSe, reducing the I_{dark}. Fig. 4(c) shows the variation of EQE with respect to the gate voltage under different power irradiation. The EQE of the photodetector reaches a maximum of 1.03×10^5% at the lowest incident power density of 1.269 mW/cm². The results demonstrate a strong photoelectric conversion capability, as evidenced by the high EQE. Fig. 4(d) shows the dependence of NEP on the incident power density at V_{ds}=6 V and V_g = -15 V. The achieved NEP value is 4.75×10^{-17} WHz$^{-1/2}$. The photoswitching characteristics at different incident powers are shown in Fig. 4(e). Under 365 nm light, the photocurrent rapidly increases and stabilises at a high value. When the light source is switched off, the photocurrent rapidly disappears. The device remains stable and variable, even after several tests, demonstrating the excellent stability and reliability of this heterojunction photodetector. This paper presents the switch characteristic curve with an optical power of 16.75 mW/cm² (Fig. 4(f)). As shown in Fig. 4(f), the response time (rise and fall) of the InSe/$MoTe_2$ heterojunction photodetector is 21.6 ms. This response speed is much improved compared to other reported heterojunction photodetectors based on grating effect[13,23,34-36].

The band gaps of $MoTe_2$ and InSe materials can be adjusted depending on their thickness, which extends the light detection range of the InSe/$MoTe_2$ heterojunction photodetector to the near-infrared. Fig. 5 shows the output characteristic curves (V_g=0 V), and the transfer characteristic curves (V_{ds}=6 V) of the InSe/$MoTe_2$ heterojunction photodetector under different incident light wavelengths. The output $I-V$ curves indicate that the photocurrent of the heterojunction photodetector increases as the drain voltage increase, The maximum photocurrent is achieved under 365 nm light irradiation.

The optical switching characteristics of InSe/$MoTe_2$ heterojunction photodetectors under different laser wave-

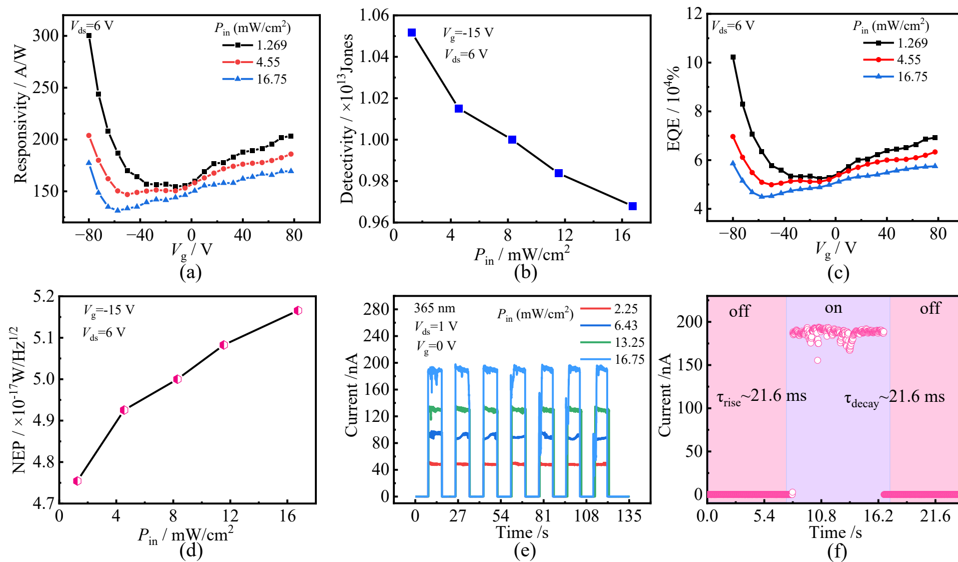

Fig. 4 (a) Responsivity as a function of the gate voltage under different incident light powers (V_{ds}=6 V); (b) Detectivity as a function of incident light power density (V_{ds}=6 V, V_g=−15 V); (c) EQE as a function of the gate voltage under different incident light powers (V_{ds}=6 V); (d) Noise equivalent power (NEP) as a function of illumination power intensity (V_g = −15 V, V_{ds}=6 V); (e) Time-dependent photocurrent response under switched-on/off light irradiation with different power intensities at V_{ds}=1 V, V_g=0 V; (f) The rise and decay times of the photocurrent under the power intensity of 16.75 mW/cm² at V_{ds}=1 V

图4 (a)不同入射光功率下的响应度与栅极电压的关系(V_{ds}=6 V);(b)探测率与入射光功率密度的函数关系(V_{ds}=6 V,V_g=−15 V);(c)外量子效率在不同入射光功率下与栅极电压的函数关系(V_{ds}=6 V);(d)噪声等效功率与入射光功率密度的函数关系(V_g = −15 V, V_{ds}=6 V);(e)不同功率强度下的光开关特性(V_{ds}=1 V,V_g=0 V);(f)光功率密度为16.75 mW/cm²时光电流的上升和衰减时间(V_{ds} = 1 V)

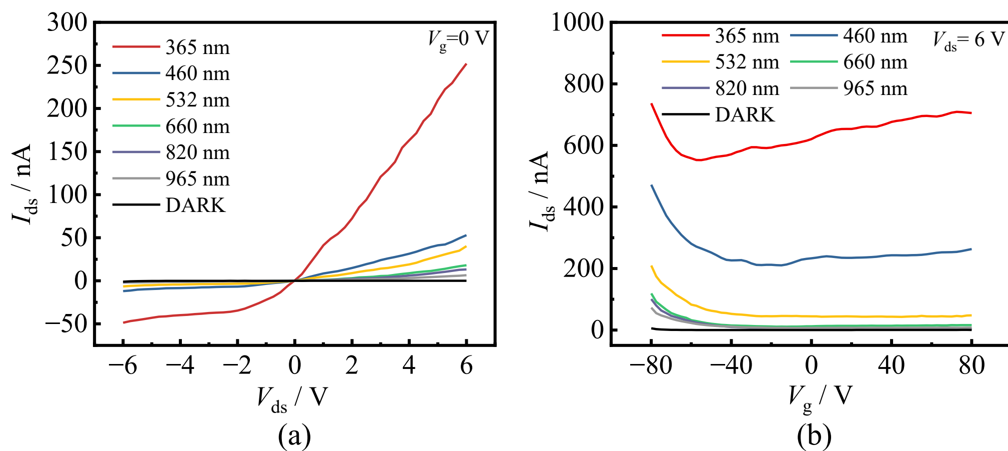

Fig. 5 (a) Photo-response of the I_{ds}-V_{ds} output characteristics (V_g = 0 V); (b) Photo-response of the I_{ds}-V_g transfer characteristics (V_{ds} = 6 V) under different incident light wavelengths.
图5 (a)不同光照波长下的I_{ds}-V_d输出特性(V_g = 0 V);(b)不同光照波长下I_{ds}-V_g转移特性曲线(V_{ds} = 6 V)

lengths are shown in Fig. 6(a). Under 365-965 nm light irradiation, the current sharply increases and remains at a high value. When the light source is switched off, the current rapidly decreases and the test results remain stable during repeated operation (see Figure S2 in the Supporting Information). It demonstrates that the heterojunction photodetector maintains excellent stability and reliability in the 365-965 nm wavelength range. The dependence of responsivity on gate voltage at different wavelengths is shown in Fig. 6(b). The device achieves its highest responsivity value at 365 nm wavelength laser within the range of -80 V to 80 V with gate voltage modulation. And the maximum value of 300. 57 A/W obtained at V_g=-80 V, indicating that the InSe/MoTe$_2$ heterojunction produces the most photogenerated electron-hole pairs under 365 nm wavelength light. Fig. 6(c) shows the dependence of D* and EQE on different incident different light wavelengths at V_{ds}=6 V and V_g = 0 V. The detectivity at 365 nm and 965 nm are 1. 25 × 10^{13} Jones and 1. 12×10^{11} Jones, respectively. The photodetector based on 2D materials has a higher result than most reported broad-spectrum photodetectors[13,35-36]. The EQE curve has a similar dependency to the detectivity curve, with a maximum EQE value of 1. 03 × 10^5% at 365 nm incident wavelength, which exceeds most of the reported photodetectors[38-39], demonstrating excellent photo conversion capability. Fig. 6(d) shows the NEP as a function of wavelength at V_{ds} = 6 V, demonstrating an ultralow noise equivalent power.

3 Conclusions

In summary, the vertically stacked InSe/MoTe$_2$ heterojunction photodetector has been fabricated and systematically investigated, where InSe serves as the grating layer to regulate the channel photocurrent through localized or released holes. In terms of photoelectric performance, the InSe/MoTe$_2$ heterojunction photodetector has a fast response time of 21. 6 ms at 365 nm, and by modulating the gate voltage and incident optical power, it can achieve a response rate of 300. 57 A/W, a maximum detectivity of 1. 05 × 10^{13} Jones, and an external quantum efficiency value of 1. 03 × 10^5%. The photodetector has excellent performance with broadband photodetection from 365 to 965 nm. Under the irradiation of 965 nm laser, the detectivity can reach of 8. 99×10^9 Jones. Our results open a way to improve photoresponsivity and reduce response time in high performance 2D optoelectronic devices.

Acknowledgment

This work is supported by the National Natural Science Foundation of China (No. 60908012, 61575008, 61775007, 61874145, 62074011, 62134008), National Key Research and Development Program of China (No. 2018YFA0209000, 2021YFC2203400, 2021YFA 1200804) , the Beijing Natural Science Foundation (No. 4172011, 4202010) and Beijing Nova Program (Z201100006820096). The authors would like to thank the Nano Fabrication Facility, Vacuum Interconnected Nanotech Workstation at Suzhou Institute of Nano-Tech and Nano-Bionics, Chinese Academy of Sciences, and Laboratory of Nanodevices and Applications, Suzhou Institute of Nano-Tech and Nano-Bionics, Chinese Academy of Sciences for their technical supports.

Reference

[1] Long M, Wang P, Fang H, *et al.* Progress, Challenges, and Opportunities for 2D Material Based Photodetectors[J]. *Advanced Functional Materials*, 2019, **29**(19): 1803807.
[2] Akinwande D, Huyghebaert C, Wang C-H, *et al.* Graphene and two-dimensional materials for silicon technology[J]. *Nature*, 2019, **573**(7775): 507-518.
[3] De Fazio D, Goykhman I, Yoon D, *et al.* High Responsivity, Large-Area Graphene/MoS$_2$ Flexible Photodetectors[J]. *ACS nano*, 2016, **10**(9): 8252-8262.
[4] Zhang W, Chiu M-H, Chen C-H, *et al.* Role of metal contacts in high-performance phototransistors based on WSe$_2$ monolayers[J]. *ACS nano*, 2014, **8**(8): 8653-8661.
[5] Yu S H, Lee Y, Jang S K, *et al.* Dye-sensitized MoS$_2$ photodetector with enhanced spectral photoresponse[J]. *ACS nano*, 2014, **8**(8): 8285-8291.

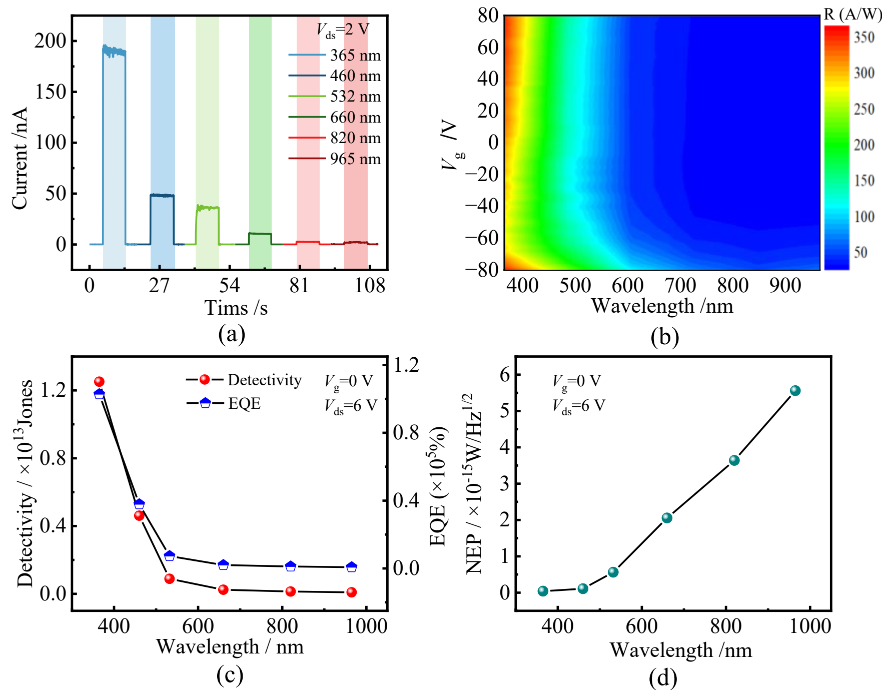

Fig. 6 (a) Time-dependent photocurrent response with different wavelengths at V_{ds} = 2 V; (b) 2D plot of responsivity as a function of incident light wavelength and gate voltage at V_{ds}=6 V; (c) D^* and EQE as a function of incident light wavelength at V_{ds}=6 V and V_g=0 V of InSe/$MoTe_2$ heterojunction photodetector; (d) Dependence of NEP on the different wavelengths at V_{ds} = 6 V and V_g = 0 V

图6 (a)不同波长照射下的光开关特性(V_{ds} = 2 V);(b)响应度随入射光波长和栅极电压变化的二维函数图像;(c)探测率和外量子效率与入射光波长的函数关系(V_{ds}=6 V, V_g=0 V)(d)噪声等效功率与不同入射光波长的函数关系

[6] Wang Y, Liu E, Gao A, *et al*. Negative Photoconductance in van der Waals Heterostructure-Based Floating Gate Phototransistor[J]. *ACS nano*, 2018, **12**(9): 9513-9520.

[7] Hu Z, Hernández-Martínez P L, Liu X, *et al*. Trion-Mediated Förster Resonance Energy Transfer and Optical Gating Effect in WS_2/hBN/$MoSe_2$ Heterojunction[J]. *ACS nano*, 2020, **14**(10): 13470-13477.

[8] Yun W S, Han S, Hong S C, *et al*. Thickness and strain effects on electronic structures of transition metal dichalcogenides: 2H-MX_2 semiconductors (M= Mo, W; X= S, Se, Te)[J]. *Phys. Rev. B*, 2012, **85**: 033305.

[9] Ruppert C, Aslan O B, Heinz T. Optical Properties and Band Gap of Single- and Few-Layer $MoTe_2$ Crystals[J]. *Nano letters*, 2014, **14**(11):6231-6236.

[10] Keum D H, Cho S, Kim J H, *et al*. Bandgap opening in few-layered monoclinic $MoTe_2$[J]. *Nature Physics*, *Nature Publishing Group*, 2015, **11**(6): 482-486.

[11] Yin L, Zhan X, Xu K, *et al*. Ultrahigh sensitive $MoTe_2$ phototransistors driven by carrier tunneling[J]. *Applied Physics Letters*, 2016, **108**(4): 043503.

[12] Pezeshki A, Shokouh S H H, Nazari T, *et al*. Electric and Photovoltaic Behavior of a Few-Layer α-$MoTe_2$/MoS_2 Dichalcogenide Heterojunction[J]. *Advanced Materials*, 2016, **28**(16): 3216-3222.

[13] Xu J, Song Y J, Park J-H, *et al*. Graphene/black phosphorus heterostructured photodetector[J]. *Solid-State Electronics*, 2018, **144**: 86-89.

[14] Chen W, Liang R, Zhang S, *et al*. Ultrahigh sensitive near-infrared photodetectors based on $MoTe_2$/germanium heterostructure[J]. *Nano Research*, 2020, **13**(1): 127-132.

[15] Huang H, Wang J, Hu W, *et al*. Highly sensitive visible to infrared $MoTe_2$ photodetectors enhanced by the photogating effect[J]. *Nanotechnology*, IOP Publishing, 2016, **27**(44): 445201.

[16] Lei S, Wen F, Ge L, *et al*. An Atomically Layered InSe Avalanche Photodetector[J]. *Nano Letters*, American Chemical Society, 2015, **15**(5): 3048-3055.

[17] Luo W, Cao Y, Hu P, *et al*. Gate Tuning of High-Performance InSe-Based Photodetectors Using Graphene Electrodes[J]. *Advanced Optical Materials*, 2015, **3**(10): 1418-1423.

[18] Mudd G W, Svatek S A, Hague L, *et al*. High Broad-Band Photoresponsivity of Mechanically Formed InSe - Graphene van der Waals Heterostructures[J]. *Advanced Materials*, 2015, **27**(25): 3760-3766.

[19] Sun Y, Gao W, Li X, *et al*. Anti-ambipolar behavior and photovoltaic effect in p-$MoTe_2$/n-InSe heterojunctions[J]. *Journal of Materials Chemistry C*, The Royal Society of Chemistry, 2021, **9**(32): 10372-10380.

[20] Yan F, Zhao L, Patanè A, *et al*. Fast multicolor photodetectors based on graphene-contacted p-GaSe/n-InSe van der Waals heterostructures[J]. *Nanotechnology*, 2017, **28**(27):27LT01.

[21] Dai M, Chen H, Wang F, *et al*. Ultrafast and Sensitive Self-Powered Photodetector Featuring Self-Limited Depletion Region and Fully Depleted Channel with van der Waals Contacts[J]. *ACS nano*, 2020, **14**(7): 9098-9106.

[22] Tao J-J, Jiang J, Zhao S-N, *et al*. Fabrication of 1D Te/2D ReS_2 Mixed-Dimensional van der Waals p-n Heterojunction for High-Performance Phototransistor[J]. *ACS nano*, 2021, **15**(2): 3241-3250.

[23] Kang B, Kim Y, Yoo W J, *et al*. Ultrahigh Photoresponsive Device Based on ReS_2/Graphene Heterostructure[J]. *Small*, 2018, **14**(45): e1802593.

[24] Tu L, Cao R, Wang X, *et al*. Ultrasensitive negative capacitance phototransistors[J]. *Nature Communications*, 2020, **11**(1): 101.

[25] Yan Y, Abbas G, Li F, *et al*. Self-Driven High Performance Broadband Photodetector Based on SnSe/InSe van der Waals Heterojunction[J]. *Advanced Materials Interfaces*, 2022, **9**(12): 2102068.

[26] Zhang Y, Li S, Li Z, *et al*. High-Performance Two-Dimensional Perovskite $Ca_2Nb_3O_{10}$UV Photodetectors[J]. *Nano Letters*, 2021, **21**(1): 382-388.

[27] Ma H, Xing Y, Han J, *et al*. Ultrasensitive and Broad-Spectrum Photodetectors Based on InSe/ReS_2 Heterostructure[J]. *Advanced Optical Materials*, 2022, **10**(5): 2101772.

[28] Huang J-H, Hsu H-H, Wang D, *et al*. Polymorphism Control of Layered $MoTe_2$ through Two-Dimensional Solid-Phase Crystallization[J]. *Scientific Reports*, 2019, **9**(1): 8810.

[29] Das S, Chen H-Y, Penumatcha A V, *et al*. High Performance Multilayer MoS_2 Transistors with Scandium Contacts[J]. *Nano Letters*, 2013, **13**(1): 100-105.

[30] Huo N, Konstantatos G. Ultrasensitive all-2D MoS_2 phototransistors enabled by an out-of-plane MoS_2 PN homojunction[J]. *Nature Communications*, 2017, **8**(1): 572.
[31] Sun Y, Song W, Gao F, *et al*. In Situ Conformal Coating of Polyaniline on GaN Microwires for Ultrafast, Self-Driven Heterojunction Ultraviolet Photodetectors [J]. *ACS Applied Materials & Interfaces*, 2020, **12**(11): 13473-13480.
[32] Zhang K, Peng M, Yu A, *et al*. A substrate-enhanced MoS_2 photodetector through a dualphotogating effect [J]. *Materials Horizons*, 2019, **6**(4): 826-833.
[33] Xu J, Rechav K, Popovitz-Biro R, *et al*. High-Gain 200 ns Photodetectors from Self-Aligned CdS-CdSe Core-Shell Nanowalls[J]. *Advanced Materials*, 2018, **30**(20): e1800413.
[34] Cao R, Wang H, Guo Z, *et al*. Black Phosphorous/Indium Selenide Photoconductive Detector for Visible and Near-Infrared Light with High Sensitivity [J]. *Advanced Optical Materials*, 2019, **7**(12): 1900020.
[35] Lan C, Li C, Wang S, *et al*. High responsive and broadband photodetectors based on WS_2-graphene van der Waals epitaxial heterostructures[J]. *J. Mater. Chem. C*, 2017, **5**: 1494-1500.
[36] Zhao D, Chen Y, Jiang W, *et al*. Gate-Tunable Photodiodes Based on Mixed-Dimensional Te/$MoTe_2$ Van der Waals Heterojunctions[J]. *Advanced Electronic Materials*, 2021, **7**(5): 2001066.
[37] Shin G, Park C, Lee K, *et al*. Ultrasensitive Phototransistor Based on WSe_2-MoS_2 van der Waals Heterojunction [J]. *Nano Letters*, 2020, **20**(8): 5741-5748.
[38] Thakar K, Mukherjee B, Grover S, *et al*. Multilayer ReS_2 Photodetectors with Gate Tunability for High Responsivity and High-Speed Applications[J]. *ACS applied materials & interfaces*, 2018, **10**(42): 36512-36522.
[39] Mukherjee B, Zulkefli M A, Hayakawa R, *et al*. Enhanced Quantum Efficiency in Vertical Mixed-thickness n-ReS_2/p-Si Heterojunction Photodiodes[J]. *ACS Photonics*, 2019, **6**(9): 2277-2286.